Predicting Erosion from Airborne Particles using a Soft-Sphere Collision Model

Cairen Miranda and John Palmore Jr
Virginia Tech,
Blacksburg, Virginia, 24061

In this study, we hypothesize that the soft-sphere collision model has the ability to simulate the erosion that occurs when airborne particles impact a surface. The key insight in this paper is to connect the particle-surface work performed during impact to the amount of erosion on the surface. This can only be done through the introduction of a new collision modeling strategy. This paper borrows the soft-sphere modeling approach from the DEM community, and uses it in a new context to model particle impact and surface erosion.

In the aerospace literature, the most commonly used collision approach is the hard-sphere model. Here the trajectories of the particles are determined by momentum-conserving binary collisions characterized by a coefficient of restitution. This model is limited in that it is not capable of predicting the physical interactions that occur simultaneously to particle impact such as surface erosion and any adhesive processes. On the other hand, the soft-sphere model is a physics-based approach which represents the particle as a Kelvin-Voigt material. The approach explicitly resolves the impact by introducing a spring-dashpot force to the governing dynamical equation for particle motion. The spring force is non-zero only when the particle is in contact with the wall.

One underexplored consequence of this approach is that it provides a time history of the particle-surface work. This information may be used in turn, to compute the amount of surface erosion. This paper uses the given information to develop a modeling approach that resolves both particle-surface collisions and surface erosion under a single framework. This model is validated using the coefficient of restitution and erosion data of Grant and Tabakoff[1, 2], which was defined for sand particles. The model is then applied to look at particle erosion on a single stage rotor-stator configuration.

I. Nomenclature

$\boldsymbol{x}$	=	Instantaneous position
t	=	Instantaneous time
m	=	Mass
$\boldsymbol{f}_p^{inter}$	=	Force acting on a single particle by the surrounding fluid
$\boldsymbol{F}_P^C$	=	Force due to particle-particle collision
$\boldsymbol{g}$	=	gravity
S	=	Surface area
$\vec{\boldsymbol{n}}$	=	Normal vector
g_r	=	Filtering kernel
$\boldsymbol{u}$	=	Fluid velocity
$\boldsymbol{F}^{inter}$	=	Particle-gas phase coupling
p	=	Hydrodynamic pressure
$\boldsymbol{I}$	=	Identity tensor
$\boldsymbol{f}^{drag}$	=	Drag force
n_p	=	Number of particles
$\vec{\boldsymbol{F}}$	=	Spring Force
k	=	Spring constant
e	=	Coefficient of Restitution
R	=	Radius

$\vec{\boldsymbol{r}}$	=	Position vector
t_e	=	Elapsed time
W	=	Surface Work
C	=	Correlation factor
K_1, K_{12}, K_3	=	Material erosion constants
f_{β_1}	=	Empirical function of particle impact angle
R_t	=	Tangential restitution ratio for Al-2024
CK	=	Constant
d	=	diameter

Greek letters

$\boldsymbol{\upsilon}$	=	Velocity vector
$\boldsymbol{\tau}$	=	Stress tensor
ϵ_f	=	Local gas volume fraction
$\mathcal{V}$	=	Volume
ρ	=	Fluid Density
μ	=	dynamic viscosity
δ	=	Spring displacement
η	=	Damping coefficient
ψ	=	Damping rate
Ω_0	=	Undamped Angular Frequency
Ω	=	Damped Angular Frequency
ε	=	Amount of erosion
β	=	Particle angle of attack
β_0	=	Angle of attack where maximum erosion occurs

Subscripts

p	=	particle
f	=	fluid
n, N	=	normal component
t, T	=	tangential component
ab	=	relative between two bodies
col	=	collision
a	=	Body A
b	=	Body B
exp	=	experimental data
0	=	Initial condition before contact
1	=	Incident properties

Superscripts

$\tilde{}$	=	Density-weighted components
$''$	=	Residual components
$\bar{}$	=	Volume filtering operation
$\vec{}$	=	Vector notation

II. Introduction

Erosion due to surface impact is a phenomenon in various particulate multi-phase engineering applications. Some common examples of this is, aircraft engines operating in areas where the air has a concentration small solid particles (like ice, sand or fly-ash), and industrial gas turbines which burn coal as fuel [3]. Erosion and deposition of sand particles on turbo-machinery adversely affect their performance [4]. Similarly aircraft flying through regions with high

concentrations of volcanic ash report reduction in performance due to erosion or deposition of ash particles [5]. Erosion is also common in pneumatic conveying systems, such as ducts and pipe elbows, which experience wear due to particle transport [6]. The wear occurring on a surface can be split into deformation due to successive particle impact and cutting damage due to surface erosion [7], of which the latter is studied in this paper. Discrete Element Method or DEM is a detailed modeling of particle-particle interactions in particle dense systems such as fluidized beds. The gas and particle phases are coupled and resolved using an Euler-Lagrangian framework [8]. DEM solves particle-particle collisions by implementing the 'soft-sphere' or 'hard-sphere model' [9]. Campbell and Brennen detailed the hard-sphere model which calculates the trajectories of the particles using momentum-conserving binary collisions [10], while the soft-sphere model which computes the contact forces by assuming a linear spring-dashpot model was developed by Cundall and Strack [11]. Approaches by Duarte et al. [12] and Lin and Chang [13] implement the hard-sphere model to solve for particle-particle collisions in wall bounded flows. Erosion due to particle motion in a channel flow under certain conditions is dominated by particle-wall collisions and so Lin and Chang developed a stochastic model to study a virtual rough wall [13], while Duarte et al. [12] define the velocities before and after contact based on the equations by [14]. There are multiple studies defining models for erosion due to particle surface impact. Peng and Cao studied implemented five different erosion models in their study [15]. They combine the rebound models of Grant and Tabakoff [2] and Forder et al. [16] along with the five erosion models to solve for erosion in a pipe bend [15].
In this study we focus on modifying the fundamental equations of the soft-sphere model to recover the predicted bounce of particles after impacting a surface as well as using those equations to solve for the erosion that occurs due to impact. The Newtonian equations of motion of the particles are used to compute the work due to impact which corresponds to the amount of erosion done on a surface. In this study, for the purpose of validation, the erosion correlation factor is based on the erosion experiment conducted by Grant and Tabakoff [2]. The hard-sphere model uses normal and tangential impulse equations to solve for the particle trajectories, as this model does not implement the Newtonian equations of motion from which we use to calculate the work done due to erosion, hence the hard sphere model cannot compute the amount of erosion from its fundamental equations.

III. Numerical Framework

In this study, an Eulerian framework is used to solve the gas phase transport equations and Lagrangian equations are used to solve the solid phase [8]. The framework uses Direct Numerical Simulation (DNS) to solve the transport equations which are represented by the Navier Stokes equations [17]. The particles are represented by discrete spherical bodies which satisfy the Lagrangian evolution equation, and are defined below,

$$\frac{d\boldsymbol{x_p}}{dt} = \boldsymbol{v_p} \tag{1}$$

$$m_p \frac{d\boldsymbol{v_p}}{dt} = \boldsymbol{f_p^{inter}} + \boldsymbol{F_p^C} + m_p \boldsymbol{g} \tag{2}$$

where, m_p represents the particle mass, the instantaneous position and velocity are denoted by, $\boldsymbol{x_p}$ and $\boldsymbol{v_p}$ respectively. The force acting on a single particle by the surrounding fluid is represented by, $\boldsymbol{f_p^{inter}}$, and the force due to particle-particle collisions is $\boldsymbol{F_p^C}$. $\boldsymbol{g}$ represents the gravity term which is 0.
The computational strategy is designed for particle-laden flow with high particle volume loading. The strategy starts from first principles by explicitly integrating the fluid forces acting on the particle surface. However, it introduces a model closure strategy to simplify the computation of these result [8]. A set of volume filtered equations for a variable density fluid, which can be solved on a scale larger than the particle diameter, was derived. Unclosed terms from the filtering approach are given in the equations below. The particle surface force consists of both Stokes drag and higher order corrections for Reynolds number and volume loading effects [18].

$$\boldsymbol{f_p^{inter}} = \int_{S_p} \boldsymbol{\tau_f} \cdot \vec{\boldsymbol{n}} d\boldsymbol{y} \tag{3}$$

S_p is the particle surface area and $\vec{\boldsymbol{n}}$ is the normal vector. where $\boldsymbol{\tau}_f$ is the fluid stress tensor. A volume filtering operation is applied to the gas phase Navier-Stokes equations to remove the effects of the microscale processes that occur on scales smaller than or equal to the particle size, and resolves the effects of processes that occur on scales larger than the particle size [8]. The filtering operation is given below,

$$\epsilon_f(\boldsymbol{x},t) = \int_{\mathcal{V}_f} g_r\left(|\boldsymbol{x}-\boldsymbol{y}|\right) d\boldsymbol{y} \tag{4}$$

where ϵ_f represents the local gas volume fraction, $\mathcal{V}_f$ indicates that the integral is taken over all points y occupied by the fluid and g_r is the filtering kernel. A density weighted volume filtering operation decomposes a quantity into its density-weighted and residual components, represented by $\widetilde{}$ and $''$ respectively. The the volume filtering operation is given by $\overline{a}$, where a represents any variable, thus $\overline{a} = \int g_r a d\boldsymbol{y}$
Eq. (5) demonstrates the filtering operation to a quantity. The volume filtered gas phase transport equations in [8] are represented by the equations below. The gas continuity equation is represented by Eq. (6), and Eq. (7) is the momentum equation.

$$\widetilde{\boldsymbol{u}} = \frac{\epsilon_f \overline{\rho \boldsymbol{u}}}{\epsilon_f \overline{\rho}} \tag{5}$$

$$\frac{\partial \epsilon_f \overline{\rho}}{\partial t} + \nabla \cdot \left(\epsilon_f \overline{\rho} \widetilde{\boldsymbol{u}}\right) = 0 \tag{6}$$

$$\frac{\partial \left(\epsilon_f \overline{\rho} \widetilde{\boldsymbol{u}}\right)}{\partial t} + \nabla \cdot \left(\epsilon_f \overline{\rho} \widetilde{\boldsymbol{u}} \otimes \widetilde{\boldsymbol{u}}\right) = \nabla \cdot \left(\overline{\boldsymbol{\tau}}_f\right) + \epsilon_f \overline{\rho} \rho \boldsymbol{g} - \boldsymbol{F}^{inter} \tag{7}$$

In Eq. (7), $\widetilde{\boldsymbol{u}}$ is the density-weight component of velocity, $\boldsymbol{F}^{inter}$ is defined as the coupling between all the particles and the gas phase, $\bar{p}$ is the volume filtered pressure, t represents time, and $\overline{\boldsymbol{\tau}}_f$ is the point wise value of the filtered fluid stress tensor and is defined in Eq. (8).

$$\overline{\boldsymbol{\tau}}_f = -\overline{p}\boldsymbol{I} + \mu\left[\nabla \overline{\boldsymbol{u}} + \nabla \overline{\boldsymbol{u}}^T - \frac{2}{3}\left(\nabla \cdot \overline{\boldsymbol{u}}\right)\boldsymbol{I}\right] \tag{8}$$

p and μ represent the hydrodynamic pressure and dynamic viscosity coefficient respectively and $\boldsymbol{I}$ is the identity tensor. The formal derivation of Eq. (7) involves additional residual stresses that are analogous to the Reynolds stresses in turbulent flows. However for this study, the mesh will be chosen fine enough so that these effects are negligible. Hence the residual stresses were neglected. $\boldsymbol{f}_p^{inter}$ can be split into volume filtered and residual components.

$$\boldsymbol{f}_p^{inter} = \int_{S_p} \boldsymbol{\tau_f} \cdot \boldsymbol{n} d\boldsymbol{y} = \int_{S_p} \left(\boldsymbol{\tau_f} + \boldsymbol{\tau_f'}\right) \cdot \boldsymbol{n} d\boldsymbol{y} \approx \mathcal{V}_p \nabla \cdot \overline{\boldsymbol{\tau}}_{\boldsymbol{f}} + \int_{S_p} \boldsymbol{\tau_f'} \cdot \boldsymbol{n} d\boldsymbol{y} \tag{9}$$

where $\mathcal{V}_p$ is the particle volume and $\left(\int_{S_p} \boldsymbol{\tau_f'} \cdot \boldsymbol{n} d\boldsymbol{y} \approx \boldsymbol{f}^{drag}\right)$, and $\boldsymbol{f}^{drag}$ is the drag force due to uniform flow which can be obtained though classical models. Therefore,

$$\boldsymbol{f}_p^{inter} \approx \mathcal{V}_p \nabla \cdot \overline{\boldsymbol{\tau}}_{\boldsymbol{f}} + \boldsymbol{f}^{drag} \tag{10}$$

$\boldsymbol{F}^{inter}$ is calculated by multiplying Eq. (3) with $g\left(\left|\boldsymbol{x}-\boldsymbol{x_p}\right|\right)$ and summing over all the particles (n_p).

$$\boldsymbol{F}^{inter} = \sum_{i=1}^{n_p} g\left(\left|\boldsymbol{x}-\boldsymbol{x_p}\right|\right) \boldsymbol{f}_p^{inter} \tag{11}$$

Eq. (11) couples the interactions between the solid and gas phases through Eq. (2) and Eq. (7), while the soft-sphere model described in Section IV accounts for particle-particle interactions.

IV. Contact Force

The collision modeling in this study borrows from the Discrete Element Method (DEM). DEM is a technique to study the macroscopic effects of the motion of particles in a fluid domain and is a more detailed modeling of particle-particle interactions, commonly used in molecular dynamic models and high density granular systems. The DEM method models particles as "hard-spheres" or as "soft-spheres" [9].
The hard-sphere and soft-sphere are the two methods of modeling particle impact. The hard-sphere model which is the standard approach used in aerospace literature implements momentum conserving equations to model the collision, and can only model binary particle-particle collisions [19]. A small timestep is required to achieve numerical stability.

The soft-sphere model which is used for more complex simulations represents the reaction between the two bodies as a spring-dashpot equation and calculates the contact force. On colliding, the particles overlap slightly to simulate deformation, and the contact forces can be calculated based on the deformation history [19]. The strategy is more numerically robust to collisions than the hard sphere model.
Fig. 1 demonstrates particle-particle collision represented by the spring-dashpot model. Particle-surface collisions can be easily represented by replacing the 2^{nd} particle with a surface. The overlap between the two bodies and is a positive value during contact and 0 at all other instants of time.

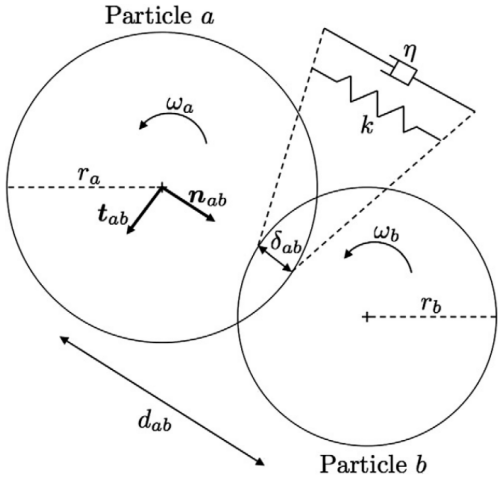

Fig. 1 Soft-Sphere Collision Model [8]

The normal contact force $\vec{\boldsymbol{F}}_n$ is computed in Eq. (12) using the spring-dashpot equation implemented in the soft-sphere collision model.

$$\vec{\boldsymbol{F}}_n = -k_n \delta_n \vec{\boldsymbol{n}}_{ab} - \eta_n \vec{\boldsymbol{v}}_{n,ab} \tag{12}$$

k_n is the normal component of the spring constant, δ_n is the overlap distance, η_n is the damping coefficient, $\vec{\boldsymbol{v}}_{n,ab}$ is the relative normal velocity between the two bodies, and $\vec{\boldsymbol{n}}_{ab}$ is the relative normal vector. The normal components of the collision is resolved using the underdamped solution to the spring-dashpot model.
The tangential force equation is analogous to Eq. (12) with $\vec{\boldsymbol{t}}_{ab}$ being the relative tangential vector.

$$\vec{\boldsymbol{F}}_t = -k_t \delta_t \vec{\boldsymbol{t}}_{ab} - \eta_t \vec{\boldsymbol{v}}_{t,ab} \tag{13}$$

This strategy contrasts to the more commonly used the static friction model, which is represented in Eq. (14) below,

$$\vec{\boldsymbol{F}}_t = -\mu_f \left|\vec{\boldsymbol{F}}_n\right| \vec{\boldsymbol{t}}_{ab} \tag{14}$$

The critically damped solution is used to solve for the tangential components. One of the drawbacks of the static friction model is that it tends to over predict the tangential force at low angles of impact [8]. In this study, the collision is spread over a large range of impact angles in a system with a low volume fraction of particles and so Eq. (13) is used to calculate the tangential contact force. Another limitation of the static friction model is that μ_f is challenging to measure via experiment. By definition, this formulation can only be used for cases that do not involve sliding or glancing impact, which precludes many impacts at low incident angles. Further, μ_f is not a true constant but is instead a complex function of the impact angle and velocity. In this work, we have chosen to directly model the tangential force rather than modeling it implicitly through the computation of μ_f. Later the advantage of this strategy will be revelealed when the spring and dashpot constants can be related to the experimentally measurable coefficient of restitution.

V. Coefficient of Restitution

The coefficient of restitution (e) is defined as the ratio of the particle velocity after impact to its velocity before impact and this coefficient can be decomposed into its normal (e_N) and tangential (e_T) components. At e = 1, the

collision is perfectly elastic while at $e < 1$, it is termed as an inelastic collision. There are a plethora of experimental studies that tabulate the coefficients of restitution of particles in various situations, Tabakoff, et al. have done several experiments resembling particles in Turbo-machinery [1, 2, 20]. The experimental setup by Hlosta, Zurovec, Rozbroj, Ramírez-Gómez, Necas, and Zegzulka consisted of a double pendulum setup with a particle attached to a cotton string to measure the coefficient of restitution for particle-particle collision [21]. While Sommerfeld and Huber conducted experiments with glass and quartz beads impacting on a rough wall [22]. Since the nature of the rebound is controlled by the forces, it seems natural to assume that the coefficients of restitution are related to the spring and dashpot constants. In the limit of low speed, elastic collisions Hertz theory [23] gives an exact relationship for coefficient of restitution based on material properties. In the current application, no such theory exists. Instead we consider the constants to be pure model constants which are chosen to recover the correct restitution coefficients. The closure strategy is summarized in this section.

A. Miranda-Palmore (MP) Model v/s Capecelatro-Desjardins (CD) Model

The numerical model to resolve the impact of particles on other particles or surfaces is introduced in Section IV. The CD model, developed by Capecelatro and Desjardins [8], follows the approach by Cundall and Strack [11], where the collision is represented by a spring-dashpot system. The MP method was developed to account for the shortcomings of the CD method, where it fails to recover the predicted coefficient of restitution at lower values. The MP method modifies the normal component of the spring constant equation so that maximum value of the spring constant occurs for a perfectly elastic collision. Both the MP and CD methods implement a 2-D soft-sphere model to solve the collision between two bodies. This method solves the contact force equation to recover the predicted coefficient of restitution with minimal error to accurately model the bounce of a particle. It should be noted that in this study we do not account for the rotation of the particle.

B. Normal Component

The fundamental equations representing particle-wall collision is presented in this section. Eq. (15) shows the normal spring displacement which is the amount of overlap between the particle and the surface, and the contact forces are non-zero only if $\delta_n \geq 0$. δ_n satisfies Eq. (15) below,

$$\delta_n = R_a - \mid \vec{r}_a - \vec{r}_b \mid \tag{15}$$

where R_a is the radius of the particle and $\mid \vec{r}_a - \vec{r}_b \mid$ is simply the distance between the particle center and the surface. The model closure for the normal spring constant k_n from Capecelatro et al [8] is shown in Eq. (16)

$$k_n = \frac{m_{ab}}{t_{col}^2}\left[\pi^2 + \ln(e_N)^2\right] \tag{16}$$

where, m_{ab} is the effective mass of the two bodies and is calculated using Eq. (17), and t_{col} is the collision time.

$$m_{ab} = \left[\frac{1}{m_a} + \frac{1}{m_b}\right]^{-1} \tag{17}$$

This model closure is termed as the Capecelatro-Desjardins (CD) model. In Eq. (16) the collision time and coefficient of restitution are assumed to be known. In a particle-surface collision, the mass for a surface is considered to be infinity and so the effective mass is the mass of just the particle, $m_{ab} = m_a$. The closure equation for η_n in Capecelatro and Desjardins [8] and van der Hoef et al. [19] represent the normal damping constant in Eq. (18)

$$\eta_n = \frac{-2\ln(e_N)\sqrt{m_{ab}k_n}}{\sqrt{\pi^2 + \ln(e_N)^2}} \tag{18}$$

A physically realistic spring constant k_n is expected to be maximum for a perfectly elastic collision which occurs at $e_N = 1$ and decreases with the decrease in e_N. However, the method [8], Eq. (16) has the opposite trend, wherein k_n approaches infinity as e_N approaches 0. Similarly, η_n maybe expected to approach 0 at $e_N = 0$, but in Eq. (18) its value tends to infinity at low e_N. An alternative approach is put forward in this paper and will be referred to as the Miranda-Palmore (MP) model in future sections.

$$t_{col} = \sqrt{\frac{m_{ab}\left(\pi^2 + \ln(e_N)\right)}{k_n}} \tag{19}$$

Rather than considering the collision time as a constant, the MP method considers it to be a function of the coefficient of restitution. The specified time scale will be shown to be the minimum collision time for all restitution coefficients. The basis of the equation is Eq. (19), which relates the collision time to the coefficient of restitution and spring constant [9]. Notice that the CD formula is apparent by inverting this relationship. However, the MP method uses a more complex algorithm toward deriving a closure for the spring constant. Eq. (19) simplifies greatly for the case of a perfectly elastic collision and can be written as,

$$t_{col,min} = \sqrt{\frac{m_{ab}\pi^2}{k_{n,max}}} \tag{20}$$

Consider the value $k_{n,max}$ to be the value of k_n that satisfies Eq. (21).

$$k_{n,max} = m_{ab}\frac{\pi^2}{t_{col,min}^2} \tag{21}$$

The collision time is made a function of the restitution coefficient by substitution of this value in Eq. (19) in place of k_n, and the equation yields,

$$t_{col}(e_N) = \sqrt{\frac{m_{ab}\left(\pi^2 + \ln(e_N)^2\right)}{k_{n,max}}} \tag{22}$$

$$t_{col}(e_N) = t_{col,min}\sqrt{1 + \left(\frac{\ln(e_N)}{\pi}\right)^2} \tag{23}$$

From the form of Eq. (23) it is clear that the collision time is minimized for perfectly elastic collisions and becomes longer for decreasing restitution coefficients. The model is completed by specifying k_n as a function of restitution coefficient. An interesting substitution is to consider the spring constant of a perfectly elastic collision that has the same collision time as Eq. (22). This substitution results in Eq. (24). The dashpot constant is closed using Eq. (18) as was done by Capercelatro and Desjardins. Howver, since the expressions for k_n are very different, the resulting values of η_n are different as well.

$$k_n = \frac{m_{ab}\pi^2}{t_{col,min}^2}\left[\frac{\pi^2}{\pi^2 + \ln(e_N)^2}\right] \tag{24}$$

Eq. (24) and Eq. (18) are model closure constants for the MP method of solving the spring-dashpot equation which model collision between two bodies. Fig. 2a and Fig. 2b represent the variation of the spring constant and damping coefficient with the normal component of restitution. Using the MP method, the normal component of the spring constant tends to 0 as the normal component of the coefficient of restitution approaches 0, as expected.

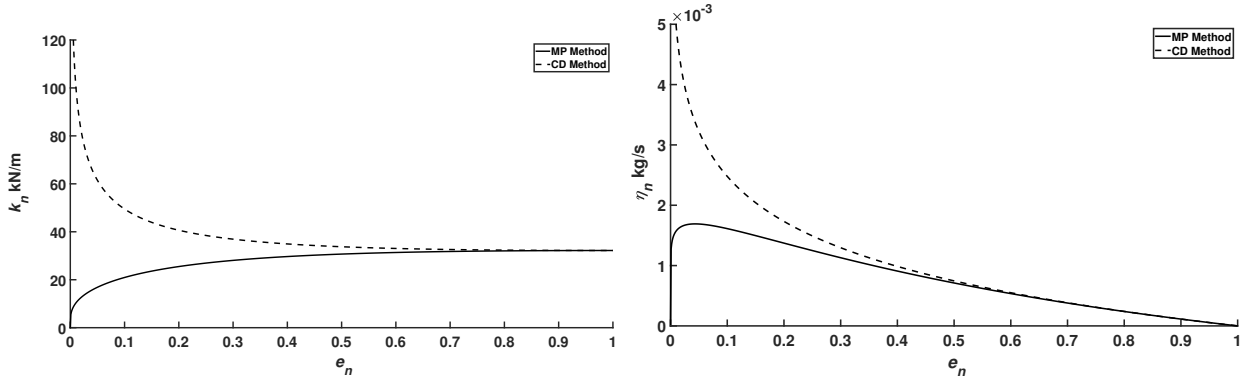

(a) e_N **vs** k_n **(b)** e_N **vs** η_n

Fig. 2 Plots showing the comparison between MP and CD techniques for k_n and η_n

C. Tangential Component

In the approach used by this work, the normal overlap for a sphere can be directly computed directly via Eq. (15). The tangential overlap is modeled based on the analytical solution to the critically damped spring dashpot Eq. (25),

$$\delta_t = \exp(\psi_t t)\, \upsilon_{0t} t \tag{25}$$

where ψ_t is defined in Eq. (26),

$$\psi_t = \frac{\eta_t}{2m_{ab}} \tag{26}$$

As was done for the normal component, in practice the values of k_t and η_t are chosen to achieve a certain value of the tangential component of the coefficient of restitution. In this case, it is easier to compute ψ_t directly from Eq. (25), and then invert to find η_t and k_t in turn. Note that at $t = t_{col}$, $\dot{\delta}_t = e_t \upsilon_{0t}$. The equation can be inverted exactly through the use of the Lambert W function, however, this function is not of common use in engineering and therefore is not found in many common software libraries. Therefore in practice it is easier to solve Eq. (26) in a computational code through the use of numerical root finding strategies such as Newton-Raphson method.

The tangential component of the coefficient of restitution can be defined as the ratio $\frac{\dot{\delta}_t(t=t_{col})}{\dot{\delta}_t(0)}$, which results in Eq. (27),

$$e_T = \exp\left(\frac{-\pi\psi_t}{\Omega_n}\right)\left[\frac{-\psi_t \pi}{\Omega_n} + 1\right] \tag{27}$$

In Eq. (27), $\Omega_n = \pi t$ at $\delta_n = 0$ [19]. The Newton-Raphson root finding technique is used to compute ψ_t for a given value of e_T. On calculating ψ_t, η_t and k_t are calculated using Eq. (28) and Eq. (29) respectively,

$$\eta_t = 2m_{ab}\psi_t \tag{28}$$

$$k_t = \Omega_{0t}^2 m_{ab} \tag{29}$$

With this the tangential contact force component is computed using Eq. (13). In Eq. (28) and Eq. (29), $\Omega_{0t} = \psi_t$, because the spring-dashpot system is critically damped. To gain the actual value of this overlap, the time since the start of collision must be known. This can be computed by inverting the analytical solution for δ_n, which is,

$$\delta_n(t) = \frac{\upsilon_0}{\Omega_n}\exp(-\psi_n t)\sin(\Omega_n t) \tag{30}$$

$$\psi_n = \frac{\eta_n}{2m_{ab}} \tag{31}$$

$$\Omega_{0n} = \sqrt{\frac{k_n}{m_{ab}}} \tag{32}$$

$$\Omega_n = \sqrt{\Omega_{0n}^2 - \psi_n^2} \tag{33}$$

Rearranging Eq. (30) with the values of ψ_n and Ω_n defined in Eqs. (31) to (33), we can calculate the elapsed time Eq. (34),

$$t_e = \frac{1}{\Omega_n} \arctan\left(\frac{\Omega_n \delta_n}{\upsilon_{0n} + \psi_n \delta_n}\right) \tag{34}$$

A suite of simulations in which a particle was injected into a domain and impacted on a flat surface at various angles was setup to measure the normal and tangential components of coefficient of restitution using the MP and CD methods. The fluid in the domain is air with a density of 1.225 kg/m^3 and has no velocity. The particle is injected into the domain at a velocity of 250 ft/s (76.2m/s) [2]. The density and diameter of the particle is 2650 kg/m^3 and 10 μm respectively, which is chosen to represent quartz which is a major component of sand. The flat plate is at an angle of 20° with respect to the horizontal in the centre of the domain. Fig. 3 displays the boundaries of the domain as well as the flat plate. The particles are injected from the left and exit through the outlet on the right, while the top and bottom act as lines of symmetry. The results of the simulation suite are displayed in Table 1 and Table 2. The simulation suite consists of setting $e_N = e_T$ for a range of values from 0.05 to 1.0 and comparing the MP and CD closure models for the normal and tangential components.

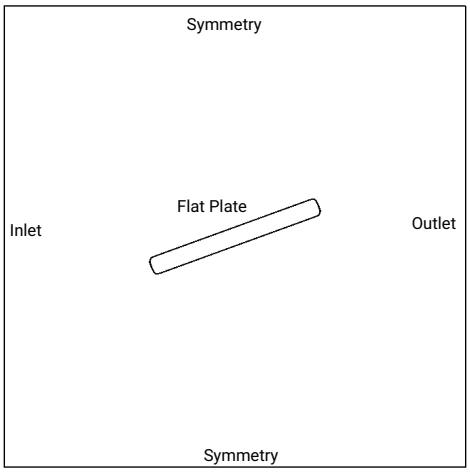

Fig. 3 Simulation Domain

Table 1 compares the e_N recovered by the MP and CD methods to the target e_N, and while the CD method is unreliable at lower e_N, the MP technique is accurate throughout the range of e_N. In Section V.C we will see that CD is just as unreliable at low e_T.

Target e_N	MP		CD	
	e_N	Error	e_N	Error
0.005	0.0047	5.792%	0.0036	28.80%
0.2	0.2032	1.601%	0.2187	9.363%
0.4	0.4210	5.248%	0.4213	5.313%
0.6	0.6272	4.525%	0.6322	5.372%
0.8	0.8282	3.528%	0.8328	4.096%
1.0	1.0417	4.170%	1.0417	4.170%

Table 1

The results discussing tangential components from simulation suite set up are displayed in Table 2 below compares the errors between the two techniques and the predicted tangential component of coefficient of restitution.

Target e_T	MP		CD	
	e_T	Error	e_T	Error
0.005	0.0045	9.643%	0.0022	55.55%
0.2	0.2001	0.030%	0.2069	3.436%
0.4	0.4035	0.885%	0.4040	0.993%
0.6	0.6015	0.244%	0.6038	0.628%
0.8	0.7975	0.309%	0.7997	0.038%
1.0	1.0000	0.003%	1.0000	0.004%

Table 2

While both methods achieve acceptable accuracy for large e_T , the CD technique is less accurate at very low e_T.

VI. Erosion

The work done on the surface by the impacting particle is the integral of the reaction force of the two bodies and is calculated using Eq. (35).

$$W = \int \vec{\boldsymbol{F}} \cdot \vec{\boldsymbol{v}} dt \tag{35}$$

On solving for the normal and tangential components of surface work, we can hypothesize that the amount of erosion is proportional to the surface work performed by the particle. Theory by Bitter [7, 24], further suggests that this work should be decomposed into contributions of work normal and tangential to the surface. Eq. (36) relates the amount of erosion to the normal and tangential components of surface work, with C_n and C_t representing the normal and tangential correlation factors respectively.

$$\varepsilon = C_n W_n + C_t W_t \tag{36}$$

In principle, C_n and C_t could be predicted from theory using material properties, but in practice, theory is currently incapable of predicting the high speed, plastic collisions relevant to this case. Hence we use the experimental data of Grant and Tabakoff [1, 2] as a reference to validate our model closure technique. Although the strategy of this paper can be used with any data set, we have chosen to rely on the well-used data of Grant and Tabakoff [1, 2] for this study.
Eq. (37) and Eq. (38) represent the predicted normal and tangential coefficients of restitution $e_{N,exp}$ and $e_{T,exp}$ as a function of the incident angle, β_1, and are created using polynomial curve fitting based on the experimental data [2]. In Fig. 3, β_1 is the angle of the rectangular wall with the horizontal as the particles enter the domain from the left in the horizontal direction.

$$e_{N,exp} = 0.993 - 1.76\beta_1 + 1.56\beta_1^2 - 0.49\beta_1^3 \tag{37}$$

$$e_{T,exp} = 0.988 - 1.66\beta_1 + 2.11\beta_1^2 - 0.67\beta_1^3 \tag{38}$$

A. Normal Component

On integrating the normal contact force $\vec{\boldsymbol{F}}_n$ in Eq. (12), the normal component of surface work W_n is calculated in Eq. (39)

$$W_n = \int \vec{\boldsymbol{F}} \cdot \vec{\boldsymbol{v}} dt = \frac{1}{2} m_{ab} \upsilon_{0n}^2 \left(1 - e_N^2\right) \tag{39}$$

Using the correlation for erosion in [2] and Eq. (39), we can obtain the normal component of the correlation factor C.

$$C_n = \frac{\varepsilon_{n,exp}}{W_n} \tag{40}$$

where, $\varepsilon_{n,exp}$ is the erosion of a perfectly normal impact with velocity υ_{0n}. The expression for C_n becomes,

$$C_n = \frac{2K_3(3.28084\upsilon_{0n})^2}{1 - e_N^2} \tag{41}$$

where $K_3 = 6e - 9$ the factor 3.28084 is included to correct the units of velocity from ft/s to m/s, which are the units used in [1, 2]. Using C_n from Eq. (41) we can obtain the modeling erosion ε_n.

$$\varepsilon_n = C_n \sum \vec{\boldsymbol{F}}_n \vec{\boldsymbol{\upsilon}}_{n,ab} dt \tag{42}$$

B. Tangential Component

The process to compute the tangential component of erosion is analogous to that of the normal component, the tangential erosion is defined as $\varepsilon_{t,exp} = \varepsilon_{exp} - \varepsilon_{n,exp}$, where ε_{exp} is the total erosion [1, 2]. The resulting expression for C_t becomes,

$$C_t = \frac{2K_1 f_{\beta_1}(1 - R_t^2)3.28084^2}{1 - e_T^2} \tag{43}$$

$$f_{\beta_1} = (1 + (CK)K_{12}\sin(2\beta_0))^2 \tag{44}$$

$$R_t = 1 - 0.0016\upsilon_{0n} \tag{45}$$

where, $K_1 = 3.67e - 3$, $K_{12} = 0.585$, β_0 is the angle of maximum erosion and $CK = 1$ if $\beta_1 \leq 2$ radian, else $CK = 0$. The tangential component of erosion can be calculated using the value of C_t from Eq. (43) in Eq. (46).

$$\varepsilon_t = C_t \sum \vec{\boldsymbol{F}}_t \vec{\boldsymbol{\upsilon}}_{t,ab} dt \tag{46}$$

Thus from Eq. (42) and Eq. (46), the amount of erosion can be calculated from the governing equations, and the collision and erosion models are both, coupled and consistent.

VII. Validation

To validate this model, we reference the setup in [2], where a flat plate is positioned at various angles of attack and a single particle is impinged on it. The experiments conducted by Grant and Tabakoff [2] are simulated, with a single spherical particle resembling sand ($d_p = 10\mu m$, $\rho_p = 2650kg/m^3$) being ejected towards a flat plate at 250 ft/s ($76.2m/s$), after which the recovered coefficient of restitution at various angles is measured. The configuration of the domain in these simulations mirrors Fig. 3. Table 3 and Table 4 compares the predicted and recovered e_N and e_T respectively while Table 5 compares the predicted erosion and the resultant erosion from simulations using the MP and CD techniques, from which we see that the MP technique is able to recover the predicted coefficients of restitution and erosion with low error percentages while the CD technique is not as accurate.

Flat Plate Angle	Predicted $e_{N,exp}$	MP		CD	
		e_N	Error	e_N	Error
20	0.5479	0.5678	3.632%	0.5777	5.449%
45	0.3356	0.3535	5.347%	0.3526	5.074%
90	0.1784	0.1829	2.516%	0.1948	9.210%

Table 3

Flat Plate Angle	Predicted $e_{T,exp}$	MP		CD	
		e_T	Error	e_T	Error
20	0.6372	0.6473	1.594%	0.6509	2.153%
45	0.6612	0.6755	2.163%	0.6749	2.065%
90	–	–	–	–	–

Table 4

Flat Plate Angle	Predicted ε_{exp} (mg)	MP		CD	
		ε (mg)	Error	ε (mg)	Error
20	1.3608e-10	1.366e-10	0.382%	1.275e-10	-6.305%
45	1.5447e-10	1.538e-10	-0.433%	1.342e-10	-13.12%
90	3.252e-11	3.398e-11	4.489%	3.453e-11	5.82%

Table 5

VIII. Particle Collision Time

One aspect that has not been discussed is the affect of the temporal integration on the numerical results of collision. In [8], they suggested that the numerical time step should be at least 15 times smaller than the particle collision time. However, there is little discussion about quantifying how the collision time affects accuracy. It is the goal of this section to determine what is the largest acceptable time step, dt, that can be used in our studies. Our work uses a 1st order time integrator based on the trapezoidal time integration scheme. Despite the use of trapezoidal scheme, our solver is temporally first order due to the strategy used for computation of $\vec{\boldsymbol{v}}_0$. Since the particle motion is measured in discrete time intervals, i.e. the time step, the exact moment of where the t_e=0 cannot be captured, so the value of $\vec{\boldsymbol{v}}_0$ is inherently an approximation. We approximate this value by taking the $\vec{\boldsymbol{v}}_0$ as being the velocity at the first time step where $\delta_n > 0$. This approach is numerically robust, but not very accurate. Hence, the overall scheme accuracy is expected to be virst order. Table 6 below shows the effects of varying $\frac{t_{col}}{dt}$ on the recovered normal coefficient of restitution (e_N).

$\frac{t_{col}}{dt}$	Predicted e_N	Recovered e_N	Error Percentage
15	1	1.156	15%
30	1	1.085	8.5%
45	1	1.055	5.5%
60	1	1.040	4%

Table 6 Timescale convergence

Another factor affected by the collision time, is the amount of compression or 'overlap' of the particle and surface. Since t_{col} is a model parameter, we choose it to ensure that the overlap remains reasonably small. Van der Hoef et al. [19] stated that an appropriate amount of compression should be limited to 1% of the diameter of the particle, i.e $\delta_n = 0.01 d_p$ for DEM studies which use the spring-dashpot model to replicate Hertzian collision. However in this paper, the soft-sphere collision strategy is introduced as an *ad hoc* modeling strategy, so the exact value of compression is arbitrary. Accordingly, we have the flexibility to limit the compression to any arbitrary value. Here, we have chosen it to be 10% of the particle diameter ($\delta_n = 0.1 d_p$).

The analytical expression for the overlap was given in Eq. (30). The first derivative of $\delta_n(t)$ is equated to 0 to find the critical point,

$$\dot{\delta}_n(t) = \frac{v_{0n}}{\Omega_n} \exp(-\psi_n t) \left(-\psi_n \sin(\Omega_n t) + \Omega_n \cos(\Omega_n t)\right) = 0 \tag{47}$$

$\exp(-\psi_n t) = 0$ cannot be a solution to the equation, as $t = -\frac{1}{\psi_n}\ln(0)$ is not a valid solution, therefore,

$$\psi_n \sin(\Omega_n t) = \Omega_n \cos(\Omega_n t) \tag{48}$$

On rearranging Eq. (48), we arrive at the solution for the time of maximum compression,

$$t_{max} = \frac{1}{\Omega_n} \arctan\left(\frac{\Omega_n}{\psi_n}\right) \tag{49}$$

Our goal will be to ensure that $\delta_n(t_{max}) = 0.1d_p$. Our modeling approach is based upon specifying restitution coefficient and collision time. Since restitution coefficient is chosen to correspond to the experimental data, this goal is essentially a statement on the choice of collision time. Substitute Eq. (49) into the expression for the overlap. Further using Eq. (18) and Eq. (24), we can substitute the values of k_n and η_n in Eqs. (31) to (33), to obtain ψ_n, Ω_{0n}, and Ω_n as functions of t_{col} and e_N.

$$\psi_n = \frac{-\pi^2}{t_{col}} \frac{1}{\pi^2 + \ln(e_N)^2} \tag{50}$$

$$\Omega_{0n} = \frac{\pi}{t_{col}} \frac{\pi}{\sqrt{\pi^2 + \ln(e_N)^2}} \tag{51}$$

$$\Omega_n = \frac{\pi^3}{t_{col}} \frac{1}{\pi^2 + \ln(e_N)^2} \tag{52}$$

Substituting Eqs. (49) to (52) in Eq. (30) and rearranging the terms, t_{col} can be written as a function of δ_n, v_{0n}, and e_N.

$$t_{col} = \frac{\delta_n \pi^3}{v_{0n}\left[\pi^2 + \ln(e_N)^2\right]} \exp\left[\frac{-\ln(e_N)}{\pi} \arctan\left(\frac{-\pi}{\ln(e_N)}\right)\right] \frac{1}{\sin\left(\arctan\left(\frac{-\pi}{\ln(e_N)}\right)\right)} \tag{53}$$

Using the MP model we plot e_N against t_{col} with a range of δ_n, in all cases, the plots have minimal values at the extreme ends of e_N, with a maximum near $e_N = 0.1$. The experimental data suggests that collision does not occur at extremely low coefficients of restitution [2]. Accordingly, for our data, the minimal value of t_{col} occurs at $e_N \to 1$ which corresponds to perfectly elastic collision.

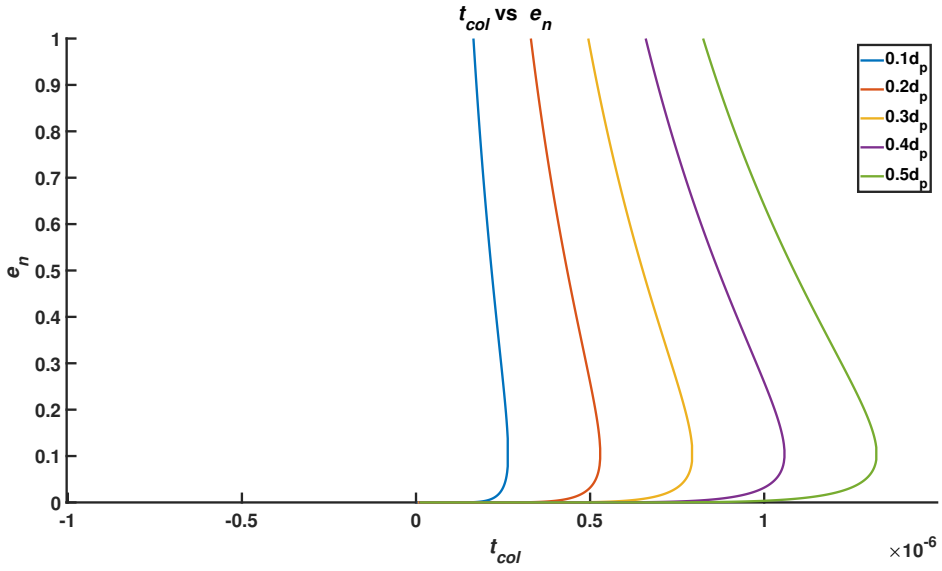

Fig. 4 Graph comparing the various δ_n on t_{col} vs e_N plot

At perfectly elastic collisions, $\psi_n = \eta_n = 0$. In that limit Eq. (53) is reduced to Eq. (54), and t_{col} can be specified by the requirement, δ_n is limited to $0.1d_p$.

$$t_{col} = \frac{\pi\delta_n}{v_{0n}} = \frac{0.1\pi d_p}{v_{0n}} \tag{54}$$

IX. Capabilities: Single Stage Compressor

A simple model of a single rotor-stator stage cascade is designed to demonstrate the capabilities of the model. In practice, the most relevant particle diameter is in the range from $10\mu m$ to $150\mu m$ and so a particle size within that range was chosen, particles with $d_p = 40\mu m$, and density, $\rho_p = 2650 kg/m^3$ are injected with an initial velocity of $76.2 m/s$ and a mass flow rate of 5e-6 kg/s at the cascade. The center of the injector from which particles enter the domain is at the midpoint inlet with a diameter of 20 mm. The fluid chosen is air which is stagnant and so the fluid velocity, $v_f = 0 m/s$. Fig. 5b below displays the capabilities of the framework in predicting the amount of erosion in mg occurring on the blade surfaces due to particle impact. The NACA 6405 airfoil was chosen to represent the rotor-stator blades. The chord length for the first stage is $1mm$ and the second stage is scaled down to 70% of the first stage. The distance between the leading edges of the rotor and stator is 0.9 mm, with the leading edge of the rotor positioned at $x = -0.75mm$ in the domain and the leading edge of the stator at $x = 0.1mm$, and the vertical distance between the airfoils are 0.8 mm. The second stage is also flipped to represent a stator. The first stage is at an angle of $-42°$ while the second stage is at an angle of $20°$. This configuration was chosen to represent a static compressor stage of an engine. With a high volume loading of particles in the domain, it is easy to visualize the erosion occuring on the airfoil surfaces. Fig. 5a demonstrates the configuration and the axes of the domain have the units of mm, while Fig. 5b shows the erosion in mg occuring on the airfoils. Particles mostly strike the suction side of the rotor stage and accordingly erosion is highest there. As particles move down stream, few hit the stator. It interesting to note that while a large range of values exist for the amount of erosion, most erosion occurs at a much lower level. Accordingly, spot damage rather than even wear is expected. A detailed study of this problem is beyond the scope of this paper, which has focused on developing the numerical technique.

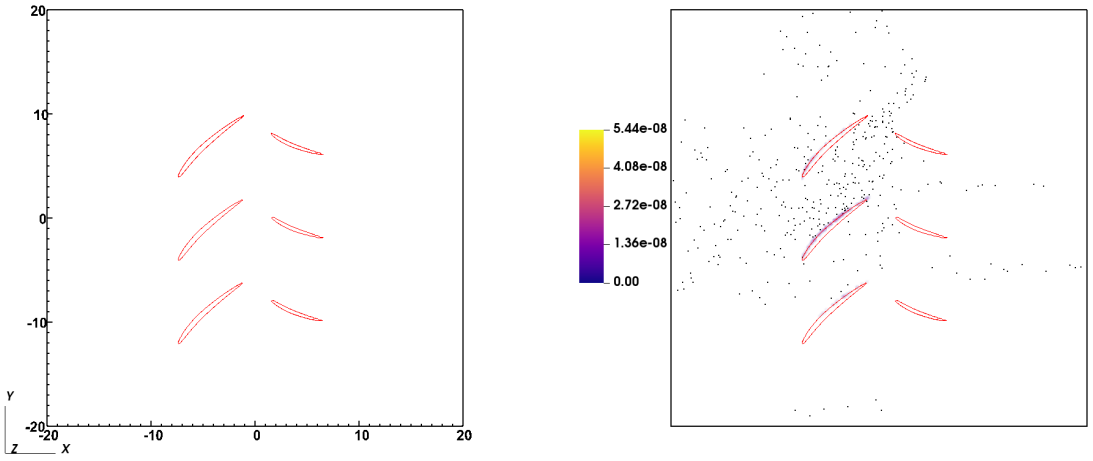

(a) The domain of rotor-stator cascade **(b) Erosion occuring on a single rotor-stator stage compressor**

Fig. 5 The domain of rotor-stator cascade along with the erosion occurring due to particle impact

X. Conclusion

This study couples the Euler-Lagragian framework [8] with the soft-sphere technique to model particle-surface collisions. The MP closure model was developed to accurately recover targeted spherical particle bounce using known values of e_N and e_T, as well as accurately predicting the amount of erosion occurring due to this particle bounce. This was done

by creating new model closure equations for k_n and η_n based on their analytical solutions. Using the fundamental equations of the soft-sphere model, the erosion that occurs due to collision is calculated. This is done by integrating the contact force equation and correlating that to the work done by erosion. The significance of the collision time along with its calculation was derived to further improve the framework while maintaining realistic physics during collision. The capabilities of the closure model were demonstrated by injecting a high volume of particles into a domain with stacked rows of airfoil to visualize the erosion due to impact.

This is a preliminary study in particle-surface impact, and future studies based on this work includes the impact dynamics of non-spherical particles on surfaces as well considering the rotational effects of these particles and implementing a 4-way coupled physics model.

References

[1] Grant, G., and Tabakoff, W., "An Experimental Investigation of the Erosive Characteristics of 2024 Aluminum Alloy," 1973.

[2] Grant, G., and Tabakoff, W., "Erosion prediction in turbomachinery resulting from environmental solid particles," *Journal of Aircraft*, Vol. 12, No. 5, 1975, pp. 471–478. https://doi.org/10.2514/3.59826.

[3] Tabakoff, W., Hamed, A., and Murugan, D. M., "Effect of target materials on the particle restitution characteristics for turbomachinery application," *Journal of Propulsion and Power*, Vol. 12, No. 2, 1996, pp. 260–266. https://doi.org/10.2514/3.24022.

[4] Hamed, A., Tabakoff, W., and Wenglarz, R., "Erosion and Deposition in Turbomachinery," *Journal of Propulsion and Power*, Vol. 22, 2006, pp. 350–360. https://doi.org/10.2514/1.18462.

[5] Clarkson, R. J., Majewicz, E. J., and Mack, P., "A re-evaluation of the 2010 quantitative understanding of the effects volcanic ash has on gas turbine engines," *Proceedings of the Institution of Mechanical Engineers, Part G: Journal of Aerospace Engineering*, Vol. 230, No. 12, 2016, pp. 2274–2291. https://doi.org/10.1177/0954410015623372, URL https://doi.org/10.1177/0954410015623372.

[6] Duarte, C. A. R., de Souza, F. J., and dos Santos, V. F., "Mitigating elbow erosion with a vortex chamber," *Powder Technology*, Vol. 288, 2016, pp. 6–25. https://doi.org/10.1016/j.powtec.2015.10.032, URL https://doi.org/10.1016/j.powtec.2015.10.032.

[7] Bitter, J., "A study of erosion phenomena part I," *Wear*, Vol. 6, No. 1, 1963, pp. 5–21. https://doi.org/https://doi.org/10.1016/0043-1648(63)90003-6, URL https://www.sciencedirect.com/science/article/pii/0043164863900036.

[8] Capecelatro, J., and Desjardins, O., "An Euler-Lagrange strategy for simulating particle-laden flows," *Journal of Computational Physics*, Vol. 238, 2013, pp. 1–31. https://doi.org/10.1016/j.jcp.2012.12.015.

[9] Deen, N., Van Sint Annaland, M., Van der Hoef, M., and Kuipers, J., "Review of discrete particle modeling of fluidized beds," *Chemical Engineering Science*, Vol. 62, No. 1, 2007, pp. 28–44. https://doi.org/10.1016/j.ces.2006.08.014, URL https://doi.org/10.1016/j.ces.2006.08.014, fluidized Bed Applications.

[10] Campbell, C. S., and Brennen, C. E., "Computer simulation of granular shear flows," *Journal of Fluid Mechanics*, Vol. 151, 1985, p. 167–188. https://doi.org/10.1017/S002211208500091X.

[11] Cundall, P. A., and Strack, O. D. L., "Discussion: A discrete numerical model for granular assemblies," *Geotechnique*, Vol. 30, No. 3, 1980, pp. 331–336. https://doi.org/10.1680/geot.1980.30.3.331.

[12] Duarte, C. A. R., de Souza, F. J., de Vasconcelos Salvo, R., and dos Santos, V. F., "The role of inter-particle collisions on elbow erosion," *International Journal of Multiphase Flow*, Vol. 89, 2017, pp. 1–22. https://doi.org/10.1016/j.ijmultiphaseflow.2016.10.001, URL https://doi.org/10.1016/j.ijmultiphaseflow.2016.10.001.

[13] Lin, J.-H., and Chang, K.-C., "Particle Dispersion Simulation in Turbulent Flow Due to Particle-Particle and Particle-Wall Collisions," *Journal of Mechanics*, Vol. 32, No. 2, 2016, p. 237–244. https://doi.org/10.1017/jmech.2015.63.

[14] Breuer, M., and Alletto, M., "Efficient simulation of particle-laden turbulent flows with high mass loadings using LES," *International Journal of Heat and Fluid Flow*, Vol. 35, 2012, pp. 2–12. https://doi.org/10.1016/j.ijheatfluidflow.2012.01.001, URL http://linkinghub.elsevier.com/retrieve/pii/S0142727X12000021.

[15] Peng, W., and Cao, X., "Numerical simulation of solid particle erosion in pipe bends for liquid–solid flow," *Powder Technology*, Vol. 294, 2016, pp. 266–279. https://doi.org/10.1016/j.powtec.2016.02.030, URL https://doi.org/10.1016/j.powtec.2016.02.030.

[16] Forder, A., Thew, M., and Harrison, D., "A numerical investigation of solid particle erosion experienced within oilfield control valves," *Wear*, Vol. 216, No. 2, 1998, pp. 184–193. https://doi.org/10.1016/S0043-1648(97)00217-2, URL https://doi.org/10.1016/S0043-1648(97)00217-2.

[17] Palmore Jr, J. A., and Desjardins, O., "Technique for forcing high Reynolds number isotropic turbulence in physical space," *Physical Review Fluids*, Vol. 3, No. 3, 2018, pp. 1–18. https://doi.org/10.1103/PhysRevFluids.3.034605, URL https://link.aps.org/doi/10.1103/PhysRevFluids.3.034605.

[18] Miranda, C., and Palmore Jr, J., "High Stokes Number Droplets in Homogeneous Isotropic Turbulent Flow," *Eastern States Section of the Combustion Institute*, 2020.

[19] van der Hoef, M. A., Ye, M., van Sint Annaland, M., Andrews, A. T., Sundaresan, S., and Kuipers, J. A., "Multiscale Modeling of Gas-Fluidized Beds," *Advances in Chemical Engineering*, Vol. 31, No. 06, 2006, pp. 65–149. https://doi.org/10.1016/S0065-2377(06)31002-2.

[20] Tabakoff, W., Malak, M. F., and Hamed, A., "Laser measurements of solid-particle rebound parameters impacting on2024 aluminum and 6A1-4V titanium alloys," *AIAA Journal*, Vol. 25, No. 5, 1987, pp. 721–726. https://doi.org/10.2514/3.9688, URL https://doi.org/10.2514/3.9688.

[21] Hlosta, J., Žurovec, D., Rozbroj, J., Álvaro Ramírez-Gómez, Nečas, J., and Zegzulka, J., "Experimental determination of particle–particle restitution coefficient via double pendulum method," *Chemical Engineering Research and Design*, Vol. 135, 2018, pp. 222–233. https://doi.org/10.1016/j.cherd.2018.05.016, URL https://doi.org/10.1016/j.cherd.2018.05.016.

[22] Sommerfeld, M., and Huber, N., "Experimental analysis and modelling of particle-wall collisions," *International Journal of Multiphase Flow*, Vol. 25, No. 6, 1999, pp. 1457–1489. https://doi.org/10.1016/S0301-9322(99)00047-6, URL https://doi.org/10.1016/S0301-9322(99)00047-6.

[23] Brogan, W., "Hertz impact between a surface and a mass-spring-mass system," *International Journal of Mechanical Sciences*, Vol. 4, No. 2, 1962, pp. 115–127. https://doi.org/https://doi.org/10.1016/S0020-7403(62)80034-4, URL https://www.sciencedirect.com/science/article/pii/S0020740362800344.

[24] Bitter, J., "A study of erosion phenomena: Part II," *Wear*, Vol. 6, No. 3, 1963, pp. 169–190. https://doi.org/https://doi.org/10.1016/0043-1648(63)90073-5, URL https://www.sciencedirect.com/science/article/pii/0043164863900735.